SnO$_2$-core carbon-shell composite nanotubes with enhanced photocurrent and photocatalytic performance

Peng Zhang [a,b], Lijie Wang [a,b], Xi Zhang [a,b], Changlu Shao [c], Junhua Hu [a,b,*], Guosheng Shao [a,b,d]

[a] School of Materials Science and Engineering, Zhengzhou University, Zhengzhou 450002, PR China
[b] International Joint Research Laboratory for Low-Carbon & Environmental Materials of Henan Province, Zhengzhou University, Zhengzhou 450002, Henan Province, PR China
[c] Center for Advanced Optoelectronic Functional Materials Research, and Key Laboratory of UV Light-Emitting Materials and Technology of Ministry of Education, Northeast Normal University, PR China
[d] Institute for Renewable Energy and Environmental Technologies, University of Bolton, Bolton BL3 5AB, UK

ARTICLE INFO

ABSTRACT

SnO$_2$-core carbon-shell composite nanotubes (SnO$_2$@C NTs) were fabricated by combining the single capillary electrospinning technique (for SnO$_2$ nanotube) and hydrothermal method (for carbon shell). The results showed that electrospun SnO$_2$ nanotubes (SNTs) were encased inside out within a uniform carbon shell about 1 nm in thickness. With respect to the SNTs, the SnO$_2$@C NTs resulted in remarkable extension of optical absorption well into the visible region. Furthermore, the photoelectrochemical performance and photocatalytic degradation activity were investigated systematically. After hybridization with carbon shell, the photocurrent of SNTs was enhanced by four times under UV irradiation and a photocurrent under visible light irradiation was observed. And, the photocatalytic studies revealed that the SnO$_2$@C NTs exhibited enhanced UV light photocatalytic efficiency and generated visible photocatalytic activity. The enhancement in performance under UV irradiation was induced by the high separation efficiency of photoinduced holes from SNTs to the HOMO of SNTs. Under visible light irradiation, the electron excited from the HOMO to the LUMO of carbon could be injected into the CB of SNTs, making SnO$_2$@C NTs present visible light photocatalytic activity. Besides, the synthesis route delivered three-dimensional sheets on the basis of interwoven nanofibrous networks, which can be readily recycled for the desirable circular application of a potent photocatalyst system.

© 2014 Elsevier B.V. All rights reserved.

1. Introduction

It has been widely demonstrated that semiconducting materials are of great promise for energy and environmental applications such as photocatalytic water splitting for hydrogen production, dye-sensitized solar cells and photocatalytic remediation of harmful organics from air and water [1–4]. As a typical n-type semiconductor, SnO$_2$ has received great attention because of its excellent stability, nontoxicity, low cost and excellent optical electricity properties [5]. Especially, the exploitations of SnO$_2$ for photocatalytic water splitting and photocatalytic oxidation of organic wastes have been hot topics because of its high reduction potential and low oxidation potential [6–8]. However, similar to other photocatalysts, the high recombination ratio of photoinduced electron–hole pairs and very poor response to visible light are still the major challenges for the enhancement of the photocatalytic efficiency of SnO$_2$ to meet the practical application requirements. Thus, some attempts have been made to reduce the recombination of photoinduced electron–hole pairs and to widen its utilization of solar light for photocatalysis, by decorating the photocatalysts with carrier scavenging agents such as noble metals (e.g. Au, Ag), metal oxides with narrower bandgaps and organic molecules [9–11].

Materials with delocalized conjugated π structures have been extensively studied in electron-transfer processes due to their rapid photoinduced charge separation and a relatively slow charge recombination. We have developed functional carbonaceous materials with conjugative π structure to enhance the photocatalytic activity of semiconductors [12–15]. In particular, it has been demonstrated successfully by different groups including ours that growing a layer of carbon on the surface of metal oxides improves

* Corresponding author at: International Joint Research Laboratory for Low-Carbon & Environmental Materials of Henan Province, Zhengzhou University, 100 Kexue Street, Zhengzhou 450052, PR China. Tel.: +863715098803.
E-mail addresses: Hujh@zzu.edu.cn (J. Hu), G.Shao@bolton.ac.uk (G. Shao).

their photocatalytic properties. [12–17] It is thus envisaged that modifying the surface of SnO_2 by carbon may also be advantageous to overcome some innate shortcomings due to either the wide band gap of, or native defects in, SnO_2. Also, carbon is an inert material and is less harmful under physiological/environmental conditions. Further, high absorption of carbon on SnO_2 may help facilitate the surfacial reactions to decompose organic pollutants. Finally, a delocalized conjugated π structure of carbon combined with SnO_2 may act as a novel "dyade" type structure which could form a common conjugated system and improve the photocatalytic activity [18–20].

Moreover, it is known that the structure and morphology also have a strong effect on the physical and chemical properties of photocatalysts, especially on the photocatalytic activities. Among various morphologies, hollow structures have attracted immense attention for their evidently improved performances over particles in photocatalysis and other applications. The hollow structures, especially those with tubular structures, have many useful features: (i) high surface-to-volume ratio enables it to adsorb a large amount of chemicals, (ii) hollow multi-channeled structures makes it convenient for mass transfer, (iii) the unique structure makes better use of light through multiple reflections within its hollow space.

Based on the above considerations, a facile method was proposed to prepare hollow SnO_2 nanotubes (SN) in this article. By surface modification with a carbon layer, an artificial photosynthetic system with core/shell structure was constructed to solve the problems of low quantum yield and poor response to visible light of SnO_2. What is more, the synthesis route delivered three-dimensional sheets on the basis of interwoven nanofibrous networks, which can be readily recycled for the desirable circular application of a potent photocatalyst system [21–25]. To date, there has been no report on the fabrication of SnO_2@C NTs (SC) core/shell photocatalyst with efficient electron–hole separation ability.

Herein, we reported a successful attempt for the fabrication the SnO_2@C NTs by combining the single capillary electrospinning technique (for SnO_2 nanotube) and hydrothermal method (for carbon layer). The photoelectrochemical performances and 4-nitrophenol (4-NP) degradation performance were investigated systematically. After hybridization with carbon, the photocurrent of SnO_2 was enhanced by four times under UV irradiation and a photocurrent under visible light irradiation was observed. The degradation results indicated that the introduction of carbon to SnO_2 can effectively enhance the UV light photocatalytic activity and also enables visible photocatalysis. Also, free-standing sheets were readily delivered using the current processing routes, which enables circular exploitation of the materials as potent environmental catalysts.

2. Experimental

2.1. Fabrication of SnO_2 nanotubes

The fabrication of SnO_2 NTs is schematically indicated in Fig. 1. To obtain nanotubes, two kinds of precursor solutions were prepared. First, certain amounts of tin dichloride dihydrate ($SnCl_2 \cdot 2H_2O$, Tianjin Chemical Corp., China) were dissolved in a mixture of 2.2 g ethanol and 2.2 g N, N-dimethyl formamide by magnetic stirring for 1 h at room temperature. Secondly, 0.4 g polyvinyl pyrrolidone (PVP, Sigma Aldrich, Mw 1 300 000) was added to the resultant solution and vigorously stirred for 3 h at room temperature. The weight ratios of PVP to $SnCl_2 \cdot 2H_2O$ was 1.78. A high voltage of 20 kV was supplied by a direct-current power supply and the feeding rate for the precursor solution was adjusted to a constant rate of 0.3 ml h^{-1} by using a syringe pump. A piece of aluminium foil was placed at 15 cm below the tip of the needle to collect the as-spun nanofibers. The process was carried out in air at RT. For the following thermolysis process, the as-spun nanofibers
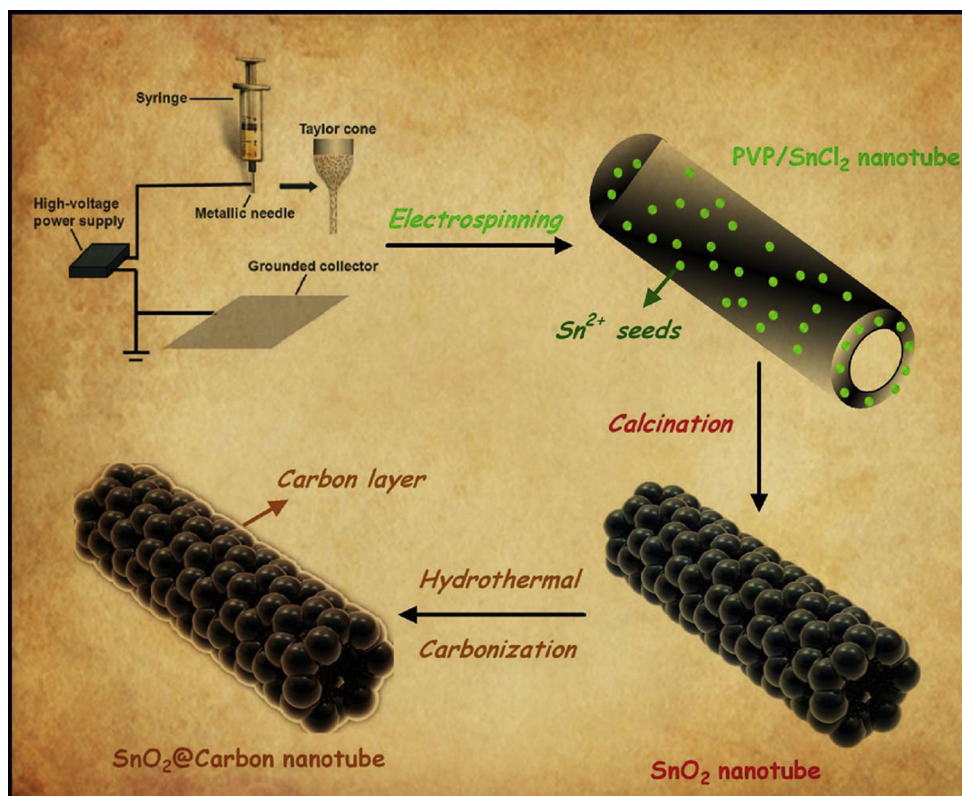

Fig. 1. Schematic illustration of the fabrication process of the SnO_2@carbon nanotubes.

Scheme 1. Postulate mechanism of the UV light and visible light-induced photodegradation of 4-NP with the SnO$_2$@carbon nanotubes.

were placed in a muffle furnace and calcined at 600 °C in air for 3 h with a heating rate of 2 °C min^{-1}, to remove PVP and obtain SnO$_2$ nanotubes.

2.2. Preparation of SnO$_2$@C NTs

In a typical experiment, as shown in Scheme 1, SnO$_2$@C NTs were prepared by hydrothermal method based on our previous work [16,17]. It was described as follows: glucose (0.1 g) and SnO$_2$ NTs (15 mg) were put into a Teflon-lined stainless steel autoclave of 25 ml capacity which contains 20 ml deionized water to make glucose solution with the concentration of 5 g l^{-1}. After vigorous stirring for 10 min, the mixture was then stirred to form a milk-like suspension, which was then sealed in the autoclave and hydrothermally treated at 180 °C for 4 h. After such reaction, the autoclave was cooled in air. The suspensions were then collected by filtration, which was washed with water for several times and dried in oven at 80 °C for 4 h. The as-fabricated sample was denoted as SC-2%. By tuning the concentration of glucose to 15 and 30 g l^{-1}, the samples of SnO$_2$@C NTs denoted as SC-5% and SC-9% were fabricated, respectively. In addition, pure SnO$_2$ NTs without carbon coatings was denoted as SN.

2.3. Characterization

The morphologies of the as-prepared nanofibers were observed by scanning electron microscopy (FESEM, JSM-7500F), transmission electron microscopy (TEM; FEI Tecnai G2 F20). X-ray diffraction (XRD) was carried out using a D/max 2500 XRD diffractometer (Rigaku) with Cu Kα radiation (0.1541 nm). The UV–vis diffuse reflectance spectroscopy was carried out using a Cary 500 UV–vis–NIR spectrophotometer. The specific surface areas of the samples were measured with a Micromeritics ASAP 2010 instrument and analyzed by the BET method. X-ray photoelectron spectroscopy (XPS) was performed on a VG-ESCALAB LKII instrument with an Mg Kα ADES (hv = 1253.6 eV) source at a residual gas pressure of below 10^{-8} Pa.

2.4. Photoelectrochemical experiment

Photoelectrochemical measurements were performed using the conventional three-electrode setup connected to an electrochemical station (CH Instrument 660 C, Shanghai Chenhua, China). The setup had pure SnO$_2$/FTO, SnO$_2$@C/FTO and carbon/FTO

(effective area was 1 cm^2) as working electrodes, and a Pt wire and an Ag/AgCl (saturated KCl) electrode were used as the counter electrode and reference electrode, respectively. The electrolyte was 0.5 M Na$_2$SO$_4$ aqueous solution. A 150 W xenon lamp with a cutoff filter (λ > 420 nm) was used as the visible light source. The photocurrent response spectroscopy was carried out at a constant potential of +0.6 V to the working photoanode. Electrochemical impedance spectra (EIS) were measured at an open-circuit voltage. A sinusoidal ac perturbation of 5 mV was applied to the electrode over the frequency range of 100 mHz to 2 MHz. Incident-photon-to-current-conversion eficiency (IPCE) spectra were measured on a QE/IPCE Measure-ment Kit (Crowntech QTest Station 1000AD) with a tungsten halogen lamp (CT-TH-150), a calibrated silicon diode and a monochromator (Crowntech QEM24-S 1/4 m).

2.5. Photocatalytic test

The photocatalytic activities were evaluated by the decomposition of 4-NP under UV light and visible light respectively. For the UV light photocatalytic test, the photoreactor was designed with an internal light source surrounded by a quartz jacket (50 W high-pressure mercury lamp with main emission wavelength of 313 nm), where a 100.0 ml of the model (4-NP) solution with an initial concentration of 10 mg l^{-1} in the presence of solid catalyst (0.01 g), respectively. For visible light photocatalytic test, the photoreactor was designed with an internal xenon lamp (XHA 150 W) equipped with a cut-off glass filter transmitting λ > 420 nm surrounded by a water-cooling quartz jacket to cool the lamp, where a 100 ml of the 4-NP solution with an initial concentration of 10 mg l^{-1} in the presence of solid catalyst (0.05 g). The solution was stirred in the dark for 30 min to obtain a good dispersion and reach adsorption–desorption equilibrium between the organic molecules and the catalyst surface. Decreases in the concentrations of 4-NP were analyzed by a Cary 500 UV–vis–NIR spectrophotometer at λ = 553 nm. At given intervals of illumination, the samples (3 ml) of the reaction solution were taken out and centrifuged. Finally, the filtrates were analyzed.

3. Results and discussion

3.1. SEM of the as-prepared composite nanofibers

The morphologies were examined by scanning electron microscopy (SEM) and representative images are shown with the
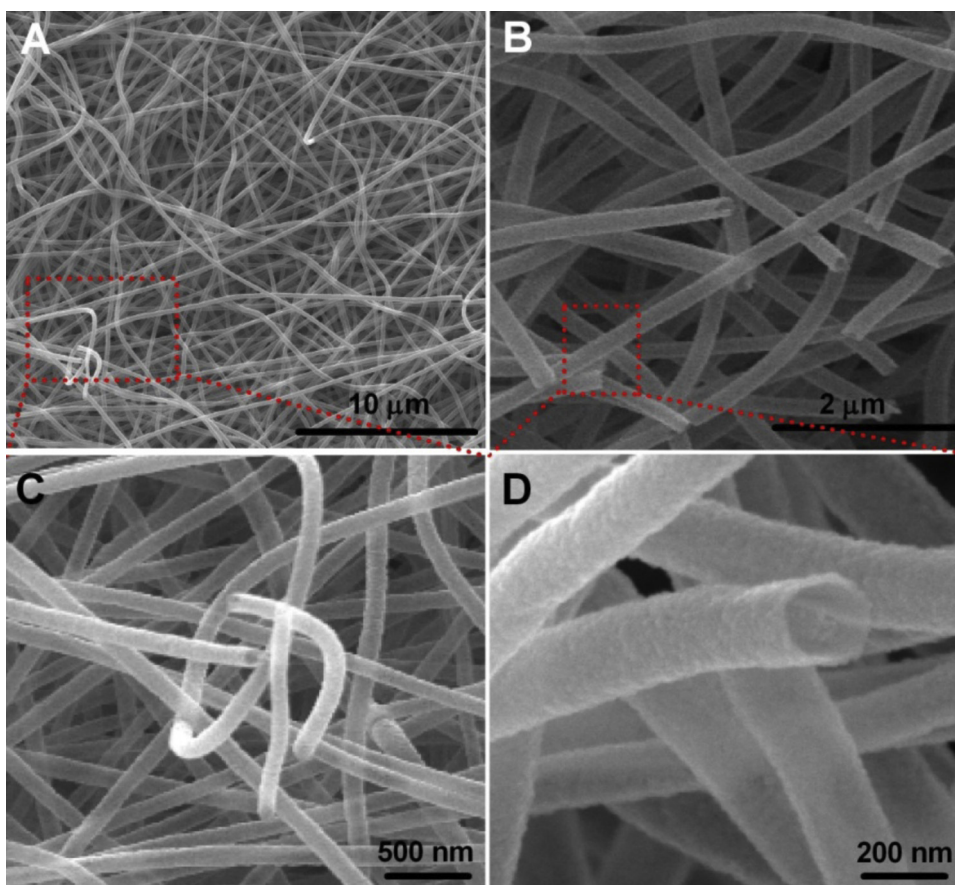
Fig. 2. SEM images of the SnO$_2$ nanotubes (A, C) and the SnO$_2$@carbon nanotubes (B, D).

as-prepared pure SnO$_2$ NTs and SnO$_2$@C NTs (SN-5%). It could be seen from Fig. 2A and C that the lengths of these randomly oriented nanotubes could reach several micrometers, and the diameters of those nanotubes ranged from 120 to 200 nm. After hydrothermal treatment, the non-woven nanotube morphology of the as-fabricated sample shown in Fig. 2B remained unchanged. Furthermore, Fig. 2D showed the high-magnification SEM image of Fig. 2B. It was observed that the SnO$_2$@C NTs had a smooth and clean surface with inner diameter of about 260 nm. In order to determine the chemical composition of the core/shell nanotube, EDX spectra (Fig. S1) of SnO$_2$@C NTs (SN-5%) in conjunction with SEM indicated that the SnO$_2$@C NTs was composed of Sn, O and C, and the Pt peak came from the conductive coating when operating the SEM. Moreover, the element content of C in the nanocomposites for all samples is listed in Table 1.

3.2. TEM of the as-prepared composite nanofibers

In order to confirm the formation of the carbon layer on SnO$_2$ NTs and to obtain more detailed information about the morphology and crystalline structure of the SnO$_2$@C NTs, the transmission electron microscopy (TEM) and high-resolution transmission electron microscopy (HRTEM) were carried out. Fig. 3A shows the typical TEM of the SnO$_2$ NTs. The SnO$_2$ NTs as core were composed of nanoparticles, and each nanoparticle attached to several other nanoparticles. In Fig. 3B, the lattice spacing is 0.335 nm, which could be assigned to the plane [1 1 0] of SnO$_2$, Compared with SnO$_2$ NTs, it could be seen from Fig. 3C and D that the carbon layer of approximately 1 nm in thickness was coated around SnO$_2$ NTs uniformly. And, as shown in Fig. 3E, it is interesting to find that the carbon layer was around the inner and outer surfaces of electrospun SnO$_2$ nanotube (SNTs). Fig. 3F displays the HRTEM image of SnO$_2$@C NTs for representation corresponding to Fig. 3D. It was clearly seen that the constituent carbon layers exhibit a layered structure and SnO$_2$@C NTs had a typical core/shell structure. It is interesting to find that the thickness of carbon layer varied linearly with the concentration of glucose, the carbon layer grew thicker to 5 and 8 nm as the concentration of glucose increased to 15.0 and 30.0 g/l, respectively (Fig. S2). And, the simultaneous presence of the crystalline SnO$_2$ and carbon crystal lattices in the region of the junction

Table 1
Physicochemical properties and weight percentage of carbon species of the samples.

Sample	Grain size[a] (nm)	Carbon content[b] (wt%)	Carbon content[c] (wt%)	S_{BET} (m^2 g^{-1})	Amount used for visible light test (g)	Amount used for UV light test (g)
SN	10.1	0	0	40.91	0.05 ± 0.002	0.01 ± 0.002
SZ-2%	9.5	2.4	2.1	40.50	0.05 ± 0.002	0.01 ± 0.002
S2-5%	9.3	5.6	5.2	41.32	0.05 ± 0.002	0.01 ± 0.002
S3-9%	9.4	9.6	8.9	40.25	0.05 ± 0.002	0.01 ± 0.002

[a] Determined by XRD using the Scherrer equation.
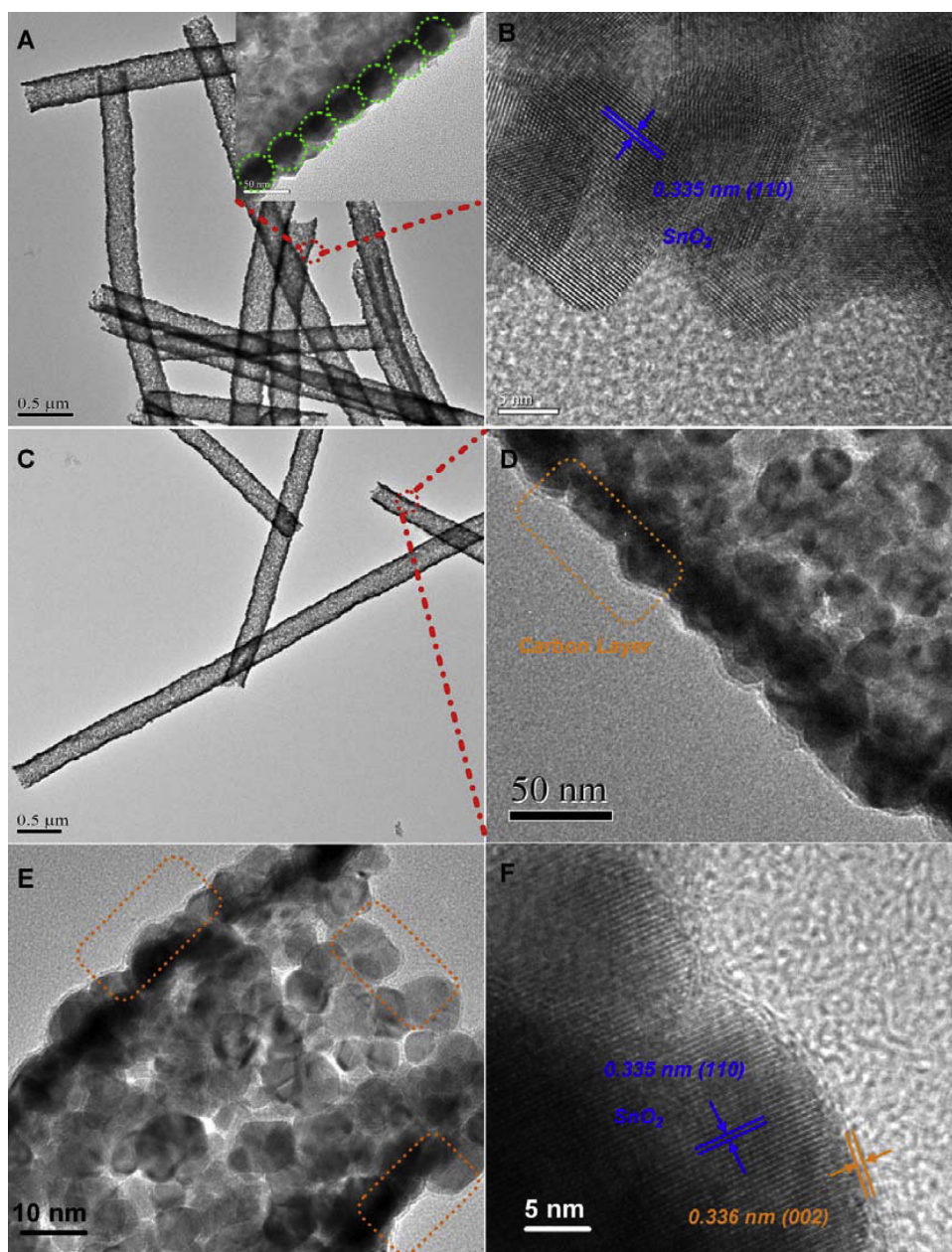[b] Determined by XPS.
[c] Determined by EDX.

Fig. 3. TEM images of the SnO$_2$ nanotube (A, B) and SnO$_2$@carbon nanotubes (C, D, E); HRTEM images of the SnO$_2$@carbon nanotubes.

were displayed. The fringe observed correspond to the interplanar distance of 0.335 nm, which agreed well with the lattice spacing of the (1 1 0) of the SNTs. Another set of the fringe spacing was ca. 0.336 nm, corresponding to the (0 0 2) plane of graphite carbon.

3.3. X-ray diffraction (XRD) patterns

X-ray diffraction (XRD) analyses were conducted to assess the carbon layer and the structure and phase purity of the SnO$_2$. As observed in Fig. 4, for pure SnO$_2$ NTs, ten reflection peaks appeared at $2\theta = 26.59°$ (1 1 0), 33.88° (1 0 1), 38.98° (2 0 0), 51.78° (2 1 1), 54.46° (2 2 0), 53.0° (4 2 2), 57.67° (0 0 2), 62.02° (3 1 0), 71.3° (2 0 2), 78.2° (3 2 1), which were attributed to the tetragonal rutile SnO$_2$ structure (space group $P42/mnm$, $a_0 = b_0 = 4.737$ Å, $c_0 = 3.186$ Å, JCPDS, No. 88-0287). And, there was no evident diffraction peak attributed to Sn and SnO secondary phases, suggesting a relatively pure SnO$_2$ phase could be obtained after calcination at 600 °C in air. The diffraction peaks of the SnO$_2$ NTs were sharp and
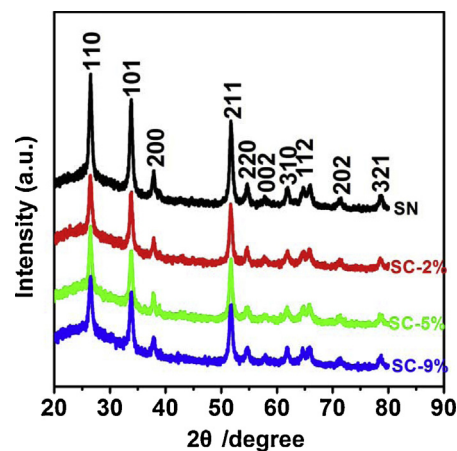

Fig. 4. XRD images of the SnO$_2$ nanotubes and SnO$_2$@carbon nanotubes.
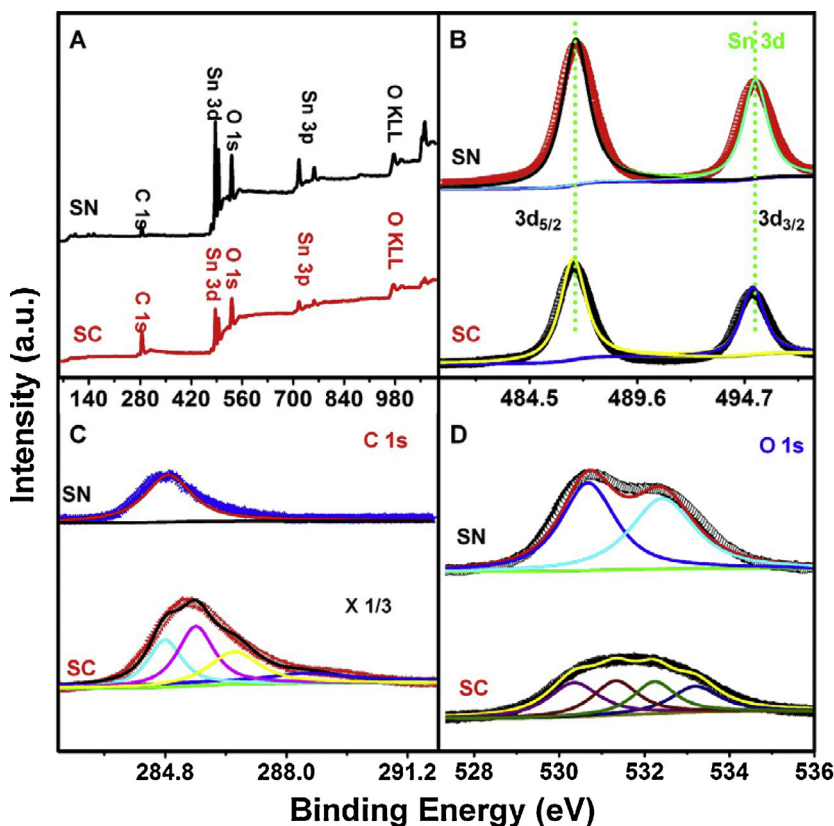
Fig. 5. XPS images of the SnO_2@carbon nanotubes.

intense, indicating good crystallinity of the nanotubes. The curves of SC-2%, SC-5% and SC-9% also exhibited the diffraction peaks of cubic phase SnO_2. And, the diffraction peak located at a 2θ value of about 25° was referred to carbon (0 0 2). The broader diffraction peak appeared to be very close to the diffraction peak characteristic to the interplanar spacing of the graphitic structure which appeared at the 2θ of about 26.5°. Based on the results, it could be indicated that the low-ordered carbon were prepared by hydrothermal processing. Notably, the lowering of the XRD peak intensity from SN to SC-9% might also be attributed to the hydrothermal processing in which the presence of glucose to some extent deteriorated the crystallinity. Moreover, the average grain sizes of the products were calculated from SnO_2 (1 1 0) peak by applying the Debye-Scherrer formula and are listed in Table 1. It could be seen that the average grain size of SnO_2 NPs was about 10 nm for all samples, which was consistent with TEM observations.

3.4. XPS spectra of the SnO_2@C NTs

Information regarding the chemical and bonding environment of the SnO_2 matrix and carbon phase was studied using X-ray photoelectron spectroscopy (XPS) [26]. The results of SnO_2 NTs and SnO_2@C NTs (SC-5%) are showed in Fig. 5 for representation. As observed in Fig. 5A, the fully scanned spectra demonstrated that Sn, O and C elements existed in both pure SnO_2 NTs and SnO_2@C NTs. The C element in pure SnO_2 could be attributed to the adventitious carbon-based contaminant. Subsequently, the Sn 3d high-resolution XPS spectra of the SnO_2 NTs and SnO_2@C NTs are analyzed in Fig. 4B. Because of the spin-orbital splits, the Sn 3d peak also had characteristic double peaks, the peaks located at 486.2 and 494.7 eV were attributed to the Sn $3d_{5/2}$ and Sn $3d_{3/2}$, respectively, and the splitting of the 3d doublet of Sn is 8.5 eV, indicated a valence state of Sn^{4+}. Besides, the peaks for

Sn 3d in the SnO_2@C NTs showed no shift compared with that in pure SnO_2 NTs, confirming that the structure of SnO_2 remained intact after coating of the carbon shell. High resolution C1s XPS spectra of SnO_2 NTs and SnO_2@C NTs are shown in Fig. 5C. For the SnO_2 NTs, the C element could be attributed to the adventitious carbon-based contaminant, and the binding energy for the C 1s peak at 284.6 eV was used as the reference for calibration. Besides the peak at 284.6 eV for SnO_2@C NTs, the three peaks at 286, 286.6 and 288 eV were characteristic of the oxygen bound species C–O, C=C and C=O, respectively. No C 1s peak at 281 eV (Sn–C bond) was observed and the chemical environments for Sn and O were not changed, strongly suggesting that carbon does not enter the SnO_2 phase. With respect to the XPS spectra of O 1s in Fig. 4D, the O 1s signal was well fitted with four contributions. The four peaks of 530.2, 531.3, 532 and 533.5 eV should be ascribed to Sn–O–Sn (lattice O), C=O (and COO), Sn–OH and C–OH (and C–O–C) species, correspondingly [12,13,27]. For pure SnO_2 NTs, there only existed two peaks which were attributed to lattice O and Sn–OH. For SnO_2@C NTs, two new oxygen signals attributed to C=O and C–OH appeared. Overall, the current XPS results indicated that the graphite carbon shell here was deposited onto the SnO_2 surface with the chemical bonds C–O–Sn, with such structuring favoring the desired charge transfer upon light excitation. And the carbon element in the form of doping, if any, must be extremely limited.

3.5. UV–vis diffuse reflectance spectra

The optical properties of the SnO_2@C NTs were probed with UV–vis diffuse reflectance spectroscopy, shown in Fig. 6. The diffuse reflectance spectrum of SnO_2 NTs only exhibited the fundamental absorption band in the UV region, and there was no more absorption in visible wavelengths. Notably, the curves of
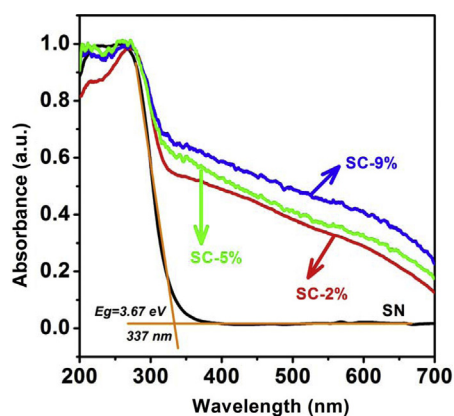
Fig. 6. DR images of the SnO_2 nanotubes and SnO_2@carbon nanotubes.

SnO_2@C NTs showed significant enhancement of light absorption at a wavelength of 400–800 nm. Further, their absorbance was enhanced in sequence from SC-2% to SC-9% following with the increase of carbon content. The reason for the absorption of visible light could be attributed to two parts: one was from the carbon itself which could absorb visible light; the other was a joint electronic system formed between SnO_2 and carbon, which gave rise in synergistic properties. The above results indicated that the sensitization of SnO_2 with carbon could extend the absorbance spectrum of SnO_2 into visible region.

3.6. Photocatalytic activity

The photocatalytic activities of the SnO_2@C NTs nanosheets were estimated by detecting the photocurrents generated and evaluated by degradation of organic pollutants 4-NP. Photocurrents were measured for SnO_2 NTs, SnO_2@C NTs and carbon electrodes under UV light and visible light, respectively (Fig. 7A and B). It was clear that fast and uniform photocurrent responses were observed in both electrodes and the photoresponsive phenomenon was entirely reversible.

Under UV light irradiation, the photocurrent of the SnO_2@C NTs electrode was about five times as high as that of the SnO_2 NTs (Fig. 7A). Under visible light irradiation, SnO_2 NTs showed almost no photocurrent response. On the contrary, SnO_2@C NTs photocatalyst showed a noticeable photocurrent under visible light irradiation (Fig. 7B). The photocurrent enhancement of the SnO_2@C NTs photocatalyst indicated an enhanced photoinduced electrons and holes separation, which could be attributed to the increased electrical conductivity. Such obviously different electrical conductivity between the SnO_2 NTs and SnO_2@C NTs can be confirmed by the electrochemical impedance spectroscopy (EIS). Fig. 7C displays the EIS of carbon, SnO_2 NTs and SnO_2@C NTs electrode. All the impedance spectra are similar, being composed of one semicircle at high frequency followed by a linear component at low frequency. There are two differences in these curves. First, in the high frequency intercept of the real axis, the internal resistances (R_b) are different. Compared with SnO_2 NTs, the R_b of SnO_2@C NTs electrode is decreased, suggesting that the carbon-rich system improve the electron conductivity of SnO_2 NTs. Second, the diffusive resistance (Warburg impedance) of the SnO_2@C NTs electrode, represented by the straight line at low frequency, is lower than that of SnO_2 NTs, suggesting a drastic decrease in the resistance of the interface and the charge transfer on the surface. It indicates that the core/shell nanotube structure of the SnO_2@C NTs can reduce the mass-transfer resistance and enhance the electrolyte penetration as well as ion diffusion in the host material because of the introduction of carbon layer with excellent electron-transporting

and electron-accepting properties. Furthermore, the SnO_2@C NTs electrode also shows a smaller charge transfer resistance (R_{ct}), which corresponds to the smaller semicircle in the impedance plots. The low R_b, R_{ct} and Warburg impedance reveal the excellent electrochemical capacitive properties of the carbon-rich material. The interfacial electron-transfer resistance of this catalyst is significantly low, probably due to the high conductivity of SnO_2@C NTs.

To further investigate the photocatalytic properties of the as-prepared photocatalyst, we also chose the 4-NP to evaluate the photocatalytic activity as it was more difficult to be degraded than the dyes in aqueous media. Fig. 7D shows the photocatalytic activity of SnO_2 NTs and the SnO_2@C NTs photocatalysts with different loading amounts of carbon under UV light. The absorption spectra variation of 4-NP vs. irradiation time on the SN-5% is shown below. The major absorption peaks of 4-NP at around 317 nm diminished gradually under UV light irradiation in the presence of SnO_2@C NTs, and the 4-NP was almost degraded fully after 40 min (Fig. S3). After UV light irradiation for 40 min, the degradation efficiencies of 4-NP were about 50, 84, 90, and 72% for the SN, SC-2%, SC-5% and SC-9%, correspondingly. Obviously, the SnO_2@C NTs showed much higher photocatalytic activities than that of pure SnO_2 NTs, while the SC-5% displayed the best photocatalytic activities among all samples. Notably, the degradation efficiency of SC-5% was higher than SC-9% with higher carbon content. A further carbon deposition seemed to have adverse effect on the carbon sensitization, which might be due to the reduced number of 4-NP molecules close to the surface of SnO_2.

Since DR spectra clearly showed that the optical response of the SnO_2@C NTs shifted into the visible-light region and SnO_2@C NTs photocatalyst showed a noticeable photocurrent under visible light irradiation, we expected that the SnO_2@C NTs present photochemical activity in the visible light region. Therefore, we also carried out experiments for the photocatalytic degradation of 4-NP under visible light irradiation. The control experiments were performed under different conditions: (i) in the presence of photocatalysts but in the dark (Fig. S4) and (ii) with visible irradiation but in the absence of the photocatalysts (Fig. S5). These control experiments revealed that there was no appreciable degradation of 4-NP over the SnO_2@C NTs in the absence of visible light irradiation, indicating that the adsorption–desorption equilibrium of 4-NP in the dark was established within 30 min. And, there was no appreciable degradation of 4-NP in the absence of photocatalysts. As shown in Fig. 8A, after visible light irradiation for 4 h, the order of photocatalytic activities is SC-5% > SC-2% > SC-9% > SN. Similar to UV photocatalytic reaction, the SnO_2@C NTs showed much higher photocatalytic activities than that of pure SnO_2 NTs. The incident photon-to-electron conversion (IPCE) spectrum is powerful to quantitatively reveal their photocatalytic activity as a function of wavelength of incident light, which is important to confirm the increased photocatalytic activity. The IPCE spectrum of SnO_2 NTs and SnO_2@C NTs in Fe^{II} was also performed and is shown in Fig. S6. Clearly, the SC sample significantly improves the photoresponse in the visible light region compared to the SN, which are consistent with their photocurrent data. Moreover, cycling use with sustaining high photocatalytic activity was a critical issue for long-term use in practical applications. Consequently, two factors need to be considered: (i) the stability of the catalyst to maintain its high activity over time. It was known that the photocorrosion or photodissolution of catalyst might occur on the photocatalyst surface in the photocatalytic reaction. To test the stability of SnO_2@C NTs, we reused the catalyst for three times. As shown in Fig. 8B, each experiment was carried out under identical conditions, and the photocatalytic activity of the SC-5% remained almost unchanged in the recycling reactions. (ii) The ease with which the catalyst could be recycled from solution. In this work, the samples were of one-
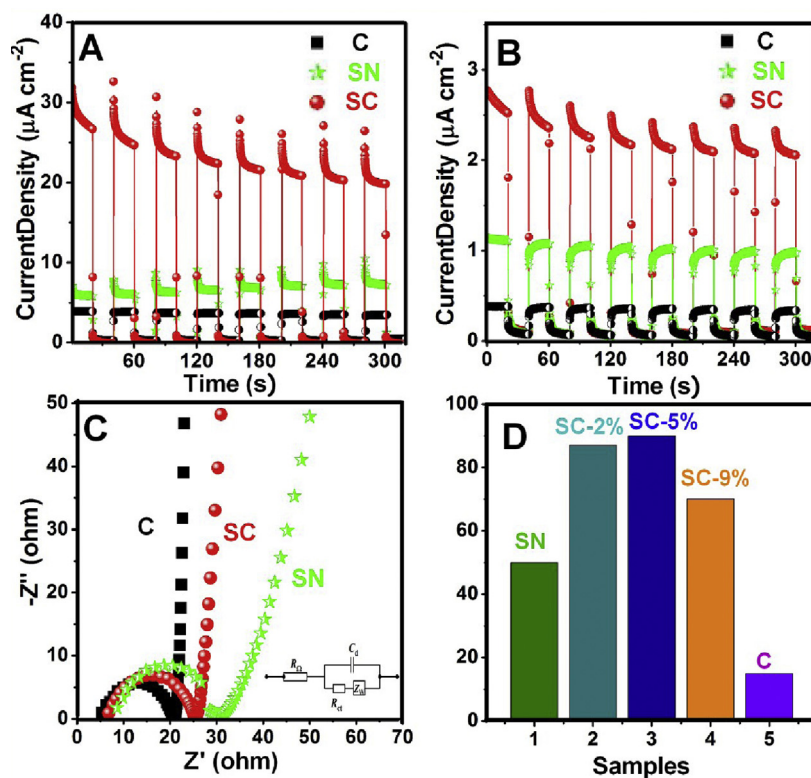
Fig. 7. (A, B) Photocurrents of C, SN and SC electrodes under visible light irradiation ($\lambda > 420$ nm) and under UV irradiation ($\lambda = 254$ nm) ([Na_2SO_4]⁻0.1 M); (C) EIS Nyquist plots of C, CN and CCN electrodes; (D) photocatalytic activity of the samples under illumination with UV light.

dimensional nanotubes morphology and could be easily separated from an aqueous suspension by sedimentation, owing to the large length to diameter ratio of the one-dimensional SnO_2@C NTs. It was indicated that the SnO_2@C NTs displayed an efficient photoactivity for the degradation of organic pollutants and could be easily recycled.

3.7. Postulated photocatalytic mechanism

On the basis of the current experimental results, possible mechanisms for UV and visible light photocatalysis are elucidated schematically in Scheme 1. The potentials of conductance and valence band (CB and VB) edges of SnO_2 were estimated via Mulliken electronegativity theory: $E_{VB} = X_{semiconductor} - E^0 + 0.5E_g$, where E_{VB} is the VB edge potential, $X_{semiconductor}$ is the electronegativity of the semiconductor, which is the geometric mean of the electronegativity of the constituent atoms, E^0 is the standard electrode potential on the hydrogen scale (ca. 4.5 eV). E_g was derived from $E_g = 1239.8/\lambda_g$, where λ_g is the absorption edge in the UV–vis spectra (shown below). The band gap energy SnO_2 NTs was 3.67 eV in this work. The conduction band (CB) and valence band (VB) for SnO_2 NTs were −0.11 and 3.56 eV, respectively. According to our previous work [12–15], we believe that there are at least two types of carbons formed on the surface of SnO_2: (1) normal C particles, acting for the electron trapping and (2) interfacial carbon (chemically bonded to SnO_2), contributing to the visible light absorption. Generally, during the photocatalytic process, the carbon shell can act as both electron acceptors and donors. Under UV light irradiation, the significant enhancement of photocurrent and photocatalytic activity was mainly due to the high efficiency of charge separation induced by the hybrid effect of SnO_2 NTs and carbon. SnO_2 can be excited by UV light and produce
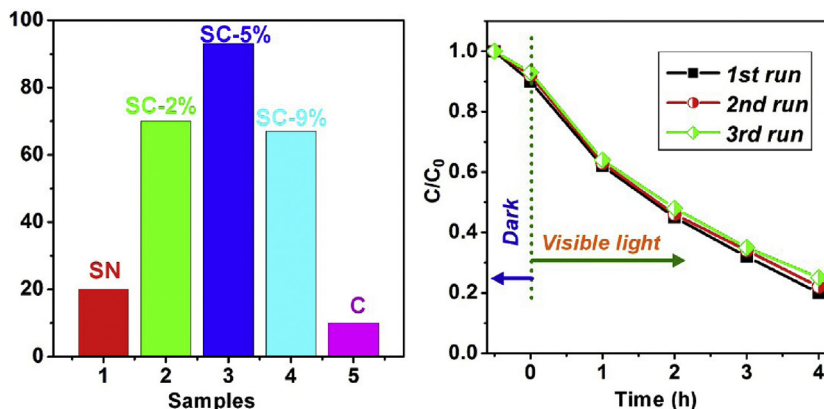

Fig. 8. (A) Photocatalytic activity of the samples under illumination with visible light. (B) Photocatalytic activity of the SnO_2@carbon nanotube with three times of cycling uses.

photogenerated electron–hole pairs to give rise to photocatalytic activity. Since the valence band (VB) position of SnO_2 is lower than the highest occupied molecular orbital (HOMO) of carbon, the photogenerated holes on SnO_2 could directly transfer to carbon, making charge separation more efficient and reducing the probability of photogenerated electron–hole recombination, leading to an enhanced photocatalytic activity [28].

Under visible light irradiation, it is well known that SnO_2 itself cannot be excited by visible light, then the graphite carbon was excited and the excited deposited carbon transferred electrons to the conductive band of SnO_2. Dissolved

$$e^- + O_2 \rightarrow O_2{}^- \tag{1}$$

$$O_2{}^- + H_2O \rightarrow HO_2\bullet + OH^- \tag{2}$$

$$HO_2\bullet + H_2O \rightarrow H_2O_2 + OH\bullet \tag{3}$$

$$H_2O_2 \rightarrow 2OH\bullet \tag{4}$$

$$OH \bullet + 4\text{-}NP \rightarrow degraded\ or\ mineralized\ products \tag{5}$$

oxygen molecules (O_2) reacted with conduction band electrons (e^-) to yield superoxide radical anions $(O_2{}^-)$ [Eq. (1)], which on protonation generated the hydroperoxy radicals (HO_2) [Eq. (2)], producing hydroxyl radicals $(OH.)$ [Eqs. (3–4)], which was a strong oxidizing agent to decompose the organic dye [29–31].

In summary, we describe herein an effective route to synthesize the $SnO_2@C$ NTs, a core/shell nanotube structure wherein a uniform carbon layer of approximately 1 nm in thickness was coated around the inner and outer surfaces of electrospun SNTs. The photoelectrochemical performances and 4-NP degradation performance were investigated systematically. After hybridization with carbon layer, the photocurrent of SNTs was enhanced by four times under UV irradiation and a photocurrent under visible light irradiation was observed. And, the photocatalytic studies revealed that the $SnO_2@C$ NTs exhibited enhanced UV light photocatalytic efficiency and generated visible photocatalytic activity. The enhancement in performance under UV irradiation was induced by the high separation efficiency of photoinduced holes from SNTs to the HOMO of SNTs. Under visible light irradiation, the electron excited from the HOMO to the LUMO of carbon could be injected into the CB of SNTs, making $SnO_2@C$ NTs present visible light photocatalytic activity. Notably, the free-standing 3D nanotubes network structure could improve photocatalyst's performance of separation and reuse. Also, it is expected that the $SnO_2@C$ NTs network will promote their industrial application as clean energy materials.

Acknowledgments

Appendix A. Supplementary data

Supplementary data associated with this article can be found, in the online version, at http://dx.doi.org/10.1016/j.apcatb.2014.11.031.

References

[1] B. O'Regan, M. Gratzel, Nature 353 (1991) 737–740.
[2] M. Batzill, Energy Environ. Sci. 4 (2011) 3275–3286.
[3] M.R. Hoffmann, S.T. Martin, W. Choi, D.W. Bahnemann, Chem. Rev. 95 (1995) 69–96.
[4] S.U. Khan, M.M. Al-Shahry, W.B. Ingler Jr., Science 297 (2002) 2243–2245.
[5] C. Zhu, P. Wang, L. Wang, L. Han, S. Dong, Nanoscale 3 (2011) 4376–4382.
[6] A. Enesca, L. Isac, L. Andronic, D. Perniu, A. Duta, Appl. Catal. B: Environ. 147 (2014) 175–184.
[7] M.H. Huang, S. Mao, H. Feick, H. Yan, Y. Wu, H. Kind, E. Weber, R. Russo, P. Yang, Science 292 (2001) 1897–1899.
[8] H. Kind, H. Yan, B. Messer, M. Law, P. Yang, Adv. Mater. 14 (2002) 158–160.
[9] Y.C. Zhang, L. Yao, G. Zhang, D.D. Dionysiou, J. Li, X. Du, Appl. Catal. B: Environ. 144 (2014) 730–738.
[10] H. Wang, S. Kalytchuk, H. Yang, L. He, C. Hu, W.Y. Teohc, A.L. Rogach, Nanoscale 6 (2014) 6084–6091.
[11] Q. Gu, J. Long, H. Zhuang, C. Zhang, Y. Zhou, X. Wang, Phys.Chem.Chem.Phys. 16 (2014) 12521–12534.
[12] P. Zhang, C. Shao, Z. Zhang, M. Zhang, J. Mu, Z. Guo, Y. Liu, Nanoscale 3 (2011) 2943–2949.
[13] P. Zhang, C. Shao, Z. Zhang, M. Zhang, J. Mu, Z. Guo, Y. Liu, J. Mater. Chem. 21 (2011) 17746–17753.
[14] P. Zhang, C. Shao, M. Zhang, Z. Guo, J. Mu, Z. Zhang, X. Zhang, P. Liang, Y. Liu, J. Hazard. Mater. 229 (2012) 265–272.
[15] P. Zhang, J. Zhang, J. Gong, Chem. Soc. Rev. 43 (2014) 4395–4422.
[16] H. Tang, C.M. Hessel, J. Wang, N. Yang, R. Yu, H. Zhao, Dan Wang, Chem. Soc. Rev. 43 (2014) 4281–4499.
[17] Y. Guo, H. Wang, C. He, L. Qiu, X. Cao, Langmuir 25 (2009) 4678–4684.
[18] L. Zhao, X.F. Chen, X.C. Wang, Y.J. Zhang, W. Wei, Y.H. Sun, M. Antonietti, M.M. Titirici, Adv. Mater. 22 (2010) 3317–3321.
[19] J. Hou, S. Jiao, H. Zhu, R.V. Kumar, CrystEngComm 13 (2011) 4735–4740.
[20] J.G. Yu, S. Wang, B. Cheng, Z. Lin, F. Huang, Catal. Sci. Technol. 3 (2013) 1782–1789.
[21] P. Zhang, C. Shao, Z. Zhang, M. Zhang, J. Mu, Z. Guo, Y. Liu, Nanoscale 3 (2011) 3357–3363.
[22] C. Zhang, S. Yu, Chem. Soc. Rev. 43 (2014) 4423–4448.
[23] P. Zhang, C. Shao, M. Zhang, Z. Guo, J. Mu, Z. Zhang, X. Zhang, Y. Liu, J. Hazard. Mater. 217 (2010) 422–428.
[24] P. Zhang, C. Shao, M. Zhang, Z. Guo, J. Mu, Z. Zhang, X. Zhang, Y. Liu, J. Hazard. Mater. 237 (2012) 331–338.
[25] Z. Zhang, C. Shao, P. Zou, P. Zhang, M. Zhang, J. Mu, Z. Guo, X. Li, C. Wang, Y. Liu, Chem. Commun. 47 (2011) 3906–3908.
[26] X. Zhou, Z. Dai, S. Liu, J. Bao, Y. Guo, Adv. Mater. 26 (2014) 3943–3949.
[27] C. Wang, C. Shao, X. Zhang, Y. Liu, Inorg. Chem. 48 (2009) 7261–7268.
[28] S. Park, S. Kim, H. Kim, C. Lee, H. Song, S. Seoa, H. Parka, D. Kim, K. Hong, J. Hazard. Mater. 275 (2014) 10–18.
[29] H. Zhang, X. Lv, Y. Li, Y. Wang, J. Li, ACS Nano 4 (2010) 380–386.
[30] L.W. Zhang, H.B. Fu, Y.F. Zhu, Adv. Funct. Mater. 18 (2008) 2180–2189.
[31] Y. Wang, R. Shi, J. Lin, Y. Zhu, Energy Environ. Sci. 4 (2011) 2922–2929.